

Article

Characteristics of Thin High Entropy Alloy Films Grown by Pulsed Laser Deposition

Edwin Alexandru Laszlo ^{1,2,3,*}, Doina Crăciun ², Gabriela Dorcioman ², Gabriel Crăciun ³, Victor Geantă ⁴, Ionelia Voiculescu ⁴, Daniel Cristea ⁵ and Valentin Crăciun ^{2,6}

¹ Faculty of Physics, University of Bucharest, 077125 Măgurele, Romania

² National Institute of R&D for Laser, Plasma & Radiation Physics, 077125 Măgurele, Romania

³ National Institute of R&D for Microtechnologies, 077190 Voluntari, Romania

⁴ Faculty of Material Science and Engineering, Polytechnic University of Bucharest, 060042 Bucharest, Romania

⁵ Faculty of Materials Science and Engineering, University of Transylvania, 500036 Braşov, Romania

⁶ Extreme Light Infrastructure for Nuclear Physics, 077125 Măgurele, Romania

* Correspondence: alexandru.laszlo@inflpr.ro

Abstract: Starting from solid-solutions (SS) of AlCoCrFeNi_x high-entropy alloys (HEAs) that have been produced with high purity constituent elements by vacuum arc remelting (VAR) method varying the nickel molar ratio x from 0.2 to 2.0, we investigated the synthesis of protective thin films of HEAs and high-entropy nitrides (HENs) with the aid of the pulsed laser deposition (PLD) system. The structure of all ten available bulk targets have been examined by means of X-Ray Diffraction (XRD), as well as their elemental composition by means of energy dispersion X-ray spectroscopy (EDS). Three targets with nickel molar composition $x = 0.4, 1.2$ and 2.0 corresponding to BCC, mixed BCC and FCC, and finally FCC structures were used for thin film depositions using a KrF excimer laser. The depositions were performed in residual low vacuum (10^{-7} mbar) and under N₂ (10^{-4} mbar) at room temperature (RT~25 °C) on Si and glass substrates. The deposited films' structure was investigated using grazing incidence XRD, their surface morphology, thickness and elemental composition by scanning electron microscopy (SEM), EDS and X-ray photoelectron spectroscopy (XPS), respectively. A homemade four-point probe (4PP) set-up was applied to determine layers electrical resistance. Besides, a Nanoindentation (NI) was employed to test films' mechanical properties. XRD results showed that all deposited films, regardless of the initial structure of targets, were a mixture of FCC and BCC structures. Additionally, the quantitative and qualitative EDS and XPS results showed that the elemental composition of films was rather close to that of the targets. The depositions under an N₂ atmosphere resulted in the inclusion of several percentage nitrogen atoms in a metallic nitride type compound into films, which may explain their higher electrical resistivity. The Young's modulus, nanohardness and friction coefficient values showed that the deposited films present good mechanical properties and could be used as protective coatings to prevent damage in harsh environments.

Keywords: high-entropy alloys; high-entropy nitrides; solid-solutions; PLD; thin-films; XRD; SEM; EDX; 4PP; NI; wear tests



Citation: Laszlo, E.A.; Crăciun, D.; Dorcioman, G.; Crăciun, G.; Geantă, V.; Voiculescu, I.; Cristea, D.; Crăciun, V. Characteristics of Thin High Entropy Alloy Films Grown by Pulsed Laser Deposition. *Coatings* **2022**, *12*, 1211. <https://doi.org/10.3390/coatings12081211>

Academic Editor: Cristian Vacacela Gomez

Received: 1 July 2022

Accepted: 14 August 2022

Published: 18 August 2022

Publisher's Note: MDPI stays neutral with regard to jurisdictional claims in published maps and institutional affiliations.



Copyright: © 2022 by the authors. Licensee MDPI, Basel, Switzerland. This article is an open access article distributed under the terms and conditions of the Creative Commons Attribution (CC BY) license (<https://creativecommons.org/licenses/by/4.0/>).

1. Introduction

Thin films are used for protective purposes of high-tech applications in many industries from nanoelectronics and medical to aerospace and nuclear. High-entropy alloys (HEAs) and their nitrides (HENs) are structural [1] and functional materials [2] that are involved in the development of the next generation of practical applications by achieving high levels of protection thanks to their outstanding properties such as improved wear, as well as corrosion resistance, and high hardness.

Hence, the focus of this paper is on the synthesis of thin films based on high-entropy AlCoCrFeNi_x alloys and high-entropy (AlCoCrFeNi_x)N nitrides [3–7], as well as on their characteristics. High entropy alloys are identified based on two definitions, namely, the

chemical elemental composition [8] on one hand, and the magnitude of systems entropy [9] on the other. Bulk solid-solutions were obtained by the VAR method, varying the nickel content of the molar ratio x from 0.2 to 2.0, upon alloying from high purity raw materials. More details about the VAR method can be found in [10]. To study the effect of nickel variation, some of the bulk SS were used as targets to grow thin films by way of the PLD technique, which has the advantage that it requires small area targets. The manuscript contains the achieved milestone regarding the growth of thin HEAs and HENs films, together with reported data on their characteristics through their study. Therefore, after the growth process the physical structure, chemical content, electric, surface, and mechanical properties of deposited thin films were analysed to understand the effect of targets' nickel content and different structure.

The novelty of our research consists of highlighting the qualities of thin alloy and nitride films that, due to their incredible characteristics, have many usages in the various industries mentioned above, such as coatings for diffusion barriers for integrated circuits, implants for human bodies, heat shields for spacecraft that re-enter in the atmosphere, or diagnostics mirrors within thermonuclear power plants, among others [11].

2. Experimental Details

Structured 3D bulk alloys that have the prefix high-entropy can be obtained by involving different manufacturing routes, such as induction melting or the Bridgeman method [12]. However, another manufacturing route to obtain bulk HEAs, namely the VAR method, was used in this research. Material losses during synthesis were low because the working chamber was vacuumed before the melting process, and the metallic bath was protected using high purity Ar 5.3 argon flow of 1.2 bar. Melting and remelting operations were performed at least five times on each side of the mini-ingots, which were obtained in the form of round tablets of about 32 mm in diameter and 9 mm in thickness. Each ingot structure was investigated by XRD with the aid of an Empyrean Panalytical multipurpose X-ray diffractometer set up to work in a Bragg–Brentano geometry with $\text{CuK}\alpha$ radiation at a power of 45 kV and 40 mA. The diffraction patterns were analysed using HighScore Plus from Panalytical and the 2021 ICCD data base.

Targets of HEAs have been mounted inside the reaction chamber, where short pulses of 25 ns were delivered by an excimer KrF laser source to irradiate their surfaces. The ablated material was collected onto substrates that were positioned parallel and at 5 cm distance with respect to targets. The glass and silicon substrates were rinsed in an ultrasonic bath in acetone ($\text{C}_3\text{H}_6\text{O}$), ethyl alcohol (ethanol- $\text{C}_2\text{H}_5\text{OH}$) and deionized water and blown dry with nitrogen gas. Films were deposited at RT at around a laser fluence of $3 \text{ J}/\text{cm}^2$, a repetition rate of 40 Hz, and a time duration of around 12 min. The films deposited under vacuum (low 10^{-7} mbar) from the targets with a nickel molar content of 0.4, 1.2 and, 2.0 were denoted as HEA2, HEA6, and respectively HEA10. Films deposited under nitrogen (10^{-4} mbar) from the same targets were denoted as HEN2, HEN6 and HEN10, respectively. Table 1 presents a summary of grown thin films.

The thin HEA and HEN films were structurally characterised by Grazing Incidence XRD (GIXRD) with the same Empyrean Panalytical multipurpose X-ray diffractometer set up to work in a parallel beam geometry. The electrical properties, which comprise the conductivity and, inversely proportional to it, the resistivity (ρ , [$\Omega \times \text{m}$]), have been assessed employing a homemade four-point probes (4PPs) electrical measurement system. The probes were connected to one voltmeter and one amperemeter, both of model KEITHLEY 6220 and 2182A. The measurement error of the whole system is in the order of 2%–3%. For each HEA and HEN of interest, values of (U/I_{\min}) were recorded, and were used together with the thickness (t) according to the formula [13]:

$$\rho = 4.53 \times U/I \times t \quad (1)$$

The microstructure and elemental composition were analysed by means of two different techniques, i.e., SEM and EDS, using a microscope Nova NanoSEM 630, and its module,

the Element EDS system. The deposited film's surface chemical composition up to a few nm depths was determined using the XPS [14,15] with an ESCALB Xi+ XPS system working with monochromatic AlK α radiation. Survey scans were initially acquired followed by high resolution scans for core level regions of Ni, Fe, Cr, Al, Co, O and N. The binding energies were referenced to adventitious C1s position at 284.8 eV.

The mechanical behaviour of thin HEA and HEN films was assessed by indentation tests to determine hardness and elastic modulus values, by micro-scratch testing to evaluate their adhesion capacity to the substrate, and by rotational wear tests to extract the dynamic friction coefficients. An NHT2 NI module from CSM Instruments/Anton Paar was used for indentation tests, using a Berkovich three-sided pyramidal diamond tip, 1 mN maximum applied load, loading and unloading sequences of 30 s, and a 5 s dwell time, to minimize the creep effect. At least 30 imprints were obtained on each sample, in various regions, and the results were averaged. The adhesion/cohesion of the thin film/substrate system was analysed with a Microscratch tester from CSM Instruments/Anton Paar, using a Rockwell geometry diamond tip (tip radius 100 μ m), linear loading to maximum 15 N, and 2 mm scratch length. Five scratch tracks were performed on each sample, followed by optical analysis to obtain the critical loads which caused either thin film fractures or partial delamination, or its complete removal. The wear behaviour was analysed with a standard tabletop tribometer from CSM Instruments/Anton Paar, using Al₂O₃ 6 mm balls as friction counterparts, in dry conditions, with a 1 N normal load and a stop condition of 200 m. Prior to wear tests, samples and friction counterparts were ultrasonically cleaned in isopropyl alcohol (isopropanol-C₃H₈O). Three wear tracks were obtained on each sample.

Table 1. Summaries of thin HEA and HEN films grown from (a) HEA2, (b) HEA6, and (c) HEA10 SS targets of crystalline structures from BCC (top) to FCC (bottom) lattice systems.

| Bulk Source | Thin Film No. | Substrate | Deposition Parameters | | | | |
|--------------|---------------|-----------|-----------------------|------------------------|---------|--------|-------------------------|
| | | | p _u (mbar) | p _{N2} (mbar) | T (min) | E (mJ) | T _{subst} (°C) |
| (a) HEA2 | 1 | Glass | 4.0×10^{-7} | 1.0×10^{-4} | 12 | 450 | RT |
| | 2 | Glass | 4.2×10^{-7} | - | 12 | 450 | RT |
| | 3 | Si | 1.9×10^{-7} | - | 12 | 450 | RT |
| | 4 | Si | 1.6×10^{-7} | 1.0×10^{-4} | 12 | 450 | RT |
| (b) HEA6 | 1 | Glass | 4.3×10^{-7} | 1.0×10^{-4} | 12 | 450 | RT |
| | 2 | Si | 1.3×10^{-7} | - | 12 | 450 | RT |
| | 3 | Si | 4.5×10^{-7} | 1.0×10^{-4} | 12 | 450 | RT |
| | 4 | Glass | 1.7×10^{-7} | - | 12 | 450 | RT |
| (c) HEA10 | 1 | Glass | 4.5×10^{-7} | - | 10 | 450 | RT |
| | 2 | Si | 1.7×10^{-7} | - | 12 | 450 | RT |
| | 3 | Si | 3.3×10^{-7} | 1.0×10^{-4} | 12 | 450 | RT |
| | 4 | Glass | 2.2×10^{-7} | 1.0×10^{-4} | 9 | 450 | RT |
| | 5 | Glass | 2.0×10^{-7} | - | 15 | 200 | RT |
| | 6 | Glass | 6.0×10^{-7} | 1.0×10^{-3} | 12 | 385 | RT |
| | 7 | Glass | 2.0×10^{-7} | 1.0×10^{-4} | 14 | 371 | RT |
| | 8 | Glass | 3.0×10^{-7} | 1.0×10^{-5} | 12 | 375 | RT |
| | 9 | Glass | 1.9×10^{-7} | - | 12 | 400 | RT |
| | 10 | Glass | 2.3×10^{-7} | - | 12 | 300 | RT |

3. Results and Discussion

The structural analysis has been carried out firstly upon all bulk SS targets with increasing nickel molar content from 0.2 up to 2.0 with a step increment of 0.2. The targets maintain the same BCC crystal structure from 0.2 up to 1.0, after which a transition occurs, where both BCC and FCC crystal phases are present, beginning with the nickel content of 1.2 up to 1.6. The observed evolution ends with the targets of the highest nickel content of 1.8 and 2.0, which presents only the FCC crystal phase (see Figure 1). Therefore, three of those targets containing 0.2, 1.2 and 2.0 were chosen as targets for thin films growth (see Figure 2).

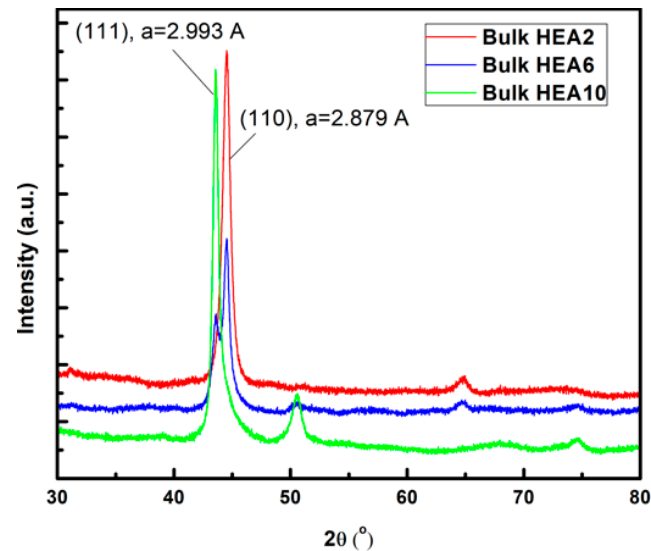


Figure 1. XRD patterns show a structural evolution of HEAs bulk SS targets from bcc (red line) to a mixed bcc-fcc structure (blue line) and finally fcc (green line) due to an increase of nickel molar content.

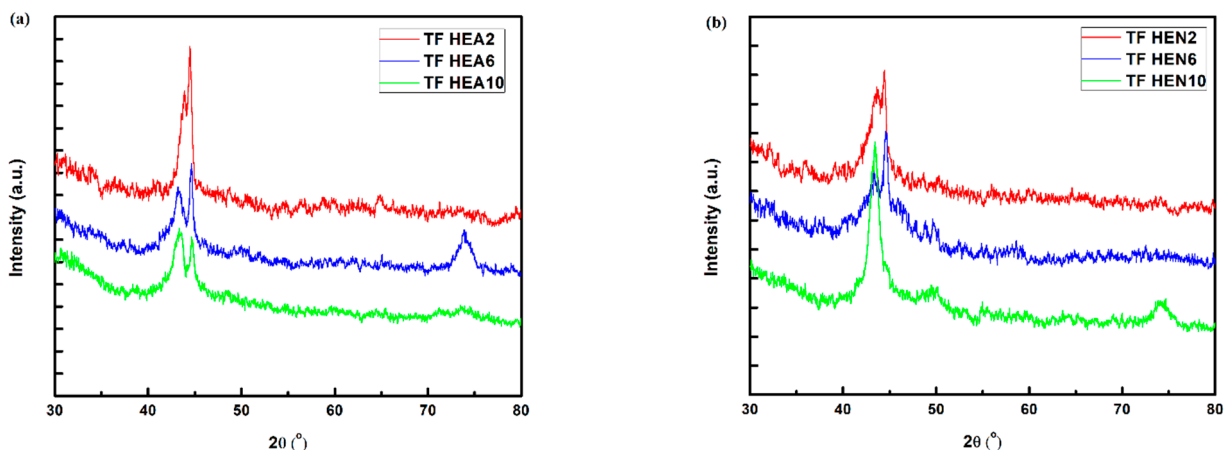


Figure 2. XRD patterns of (a) the analysed thin HEA films and (b) the analysed thin HEN films, both containing different nickel molar content, 0.4, 1.2, and 2.0. TF stands for thin film.

As one can see in Figure 1, the HEA targets containing a low nickel concentration crystallized in the BCC lattice. As the nickel molar content increased to $x = 1.0$ and above, a mixed structure containing both BCC and FCC lattices appeared. For nickel molar concentration $x = 1.8$ and higher only the FCC lattice was observed. The chosen targets for thin films growth corresponded to these three different crystalline structures, pure BCC ($x = 0.4$), mixed BCC and FCC ($x = 1.2$) and pure FCC ($x = 2.0$). The deposited films

always exhibited a mixed crystalline structure, as shown in Figure 2. From the acquired XRD patterns the grain sizes and lattice parameters have been assessed using the Scherrer equation, corrected for the instrumental broadening, and Bragg's law. The values obtained are presented in Table 2. The results of electrical resistivity measurements conducted by the aforementioned 4PP system, taking into account the films thicknesses estimated from cross-section SEM images (see Figure 5) are displayed in Table 3. The obtained resistivity values are similar to other values reported in the literature for this HEA system. It is also evident that the resistivity values are higher for films deposited under an N₂ atmosphere.

Table 2. Summary of physical parameter values determined for indicated thin films.

| Bulk Source | Thin Film No. | Grain Size [Å] | Lattice Parameter [Å] |
|-------------|---------------------|------------------------|----------------------------|
| HEA2 | (target) | 90 (bcc) | 2.879 (bcc) |
| | 1 (N ₂) | 112 (bcc) 37 (fcc) | 2.884 (bcc) 3.008 (fcc) |
| | 2 (vacuum) | 208 (bcc) 66 (fcc) | 2.879 (bcc) 2.981 (fcc) |
| HEA6 | (target) | 114 (bcc) 112 (fcc) | 2.879 (bcc) 2.995 (fcc) |
| | 1 (N ₂) | 145 (bcc) 38 (fcc) | 2.874 (bcc) 3.017 (fcc) |
| | 4 (vacuum) | 142 (bcc) 62 (fcc) | 2.872 (bcc) 3.015 (fcc) |
| HEA10 | (target) | 117 (fcc) | 2.993 (fcc) |
| | 4 (N ₂) | 52 (fcc) | 3.006 (fcc) |
| | 1 (vacuum) | 182 (bcc) 41 (fcc) | 2.865 (bcc) 3.015 (fcc) |

Table 3. Summary of HEA and HEN thin films thicknesses, values of U/I_{min} and resistivities.

| Bulk Source | Thin Film No. | Thickness, t [m] | (U/I) _{min} [mV/mA] | R _s [Ω] | Resistivity, ρ [μΩ-cm] |
|-------------|---------------------|-------------------------|------------------------------|--------------------|------------------------|
| HEA2 | 2 (vacuum) | 1.77 × 10 ⁻⁷ | 1.31 | 5.93 | 105.3 |
| | 4 (N ₂) | 2.32 × 10 ⁻⁷ | 1.43 | 6.48 | 150.6 |
| HEA6 | 2 (vacuum) | 1.37 × 10 ⁻⁷ | 1.72 | 7.79 | 106.7 |
| | 3 (N ₂) | 2.66 × 10 ⁻⁷ | 1.61 | 7.29 | 194.1 |
| HEA10 | 2 (vacuum) | 1.19 × 10 ⁻⁷ | 1.67 | 7.56 | 90.4 |
| | 4 (N ₂) | 1.64 × 10 ⁻⁷ | 1.71 | 7.75 | 127.2 |

Surface morphology analyses were carried out by SEM. Typical surface images acquired from thin HEA6 and HEN6 film at different magnifications are displayed in Figures 3 and 4. Moreover, thicknesses of the deposited films were measured on the cross-section of fractured samples by means of this technique. As one can see, regardless of deposition conditions, thin films exhibit micrometer size droplets that are usual when the PLD system is employed. Moreover, on some surfaces, sites where droplets used to be attached and now were detached can be seen. On some other surfaces, droplets that stacked on top of each other were observed. Besides, some droplets turned into donut shaped ones due to a hydrodynamic effect during impingement into the substrate and then cooling. There were no significant morphological changes between images acquired from thin HEA6 and HEN6 film.

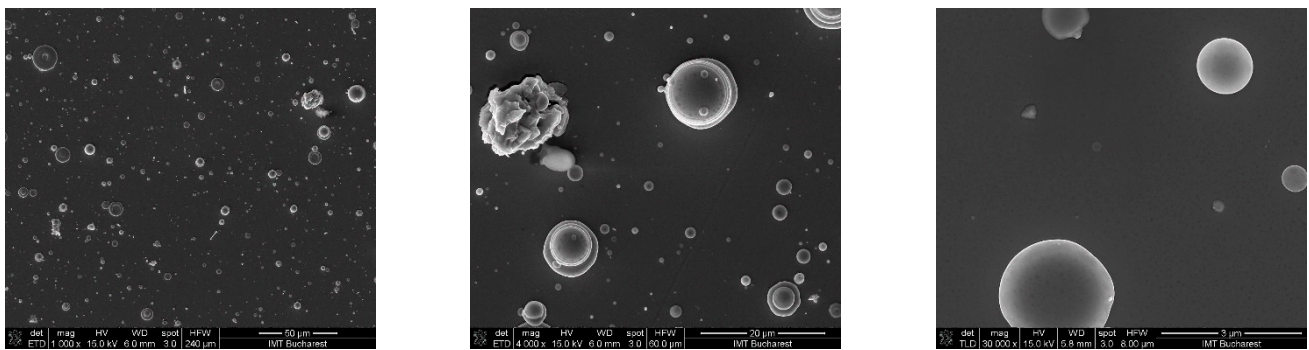


Figure 3. Typical SEM images of the surface morphology of a HEA6 thin film at different magnifications: 1000 \times , 4000 \times , and 30,000 \times , from left to right, respectively.

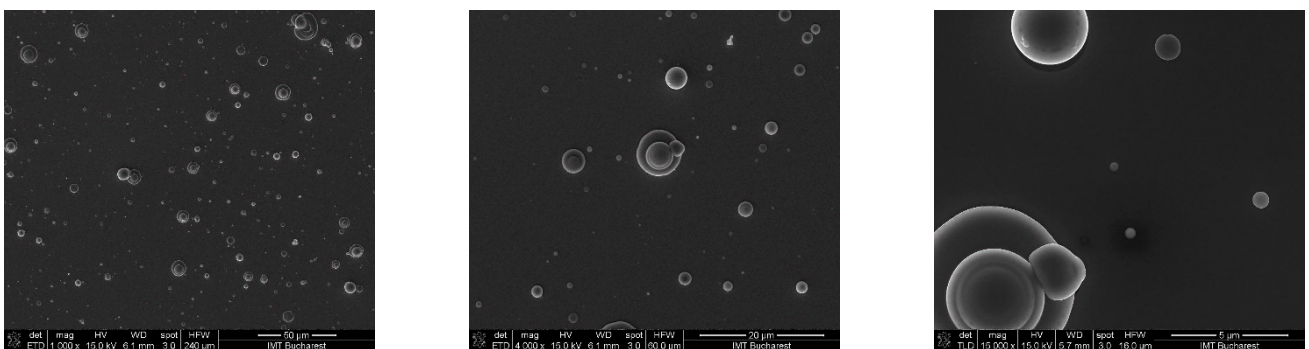


Figure 4. Typical SEM images of the surface morphology of a HEN6 thin film at different magnifications: 1000 \times , 4000 \times , and 15,000 \times , from left to right, respectively.

Thickness analyses have been carried out with samples positioned at 45° from the horizontal position, so that the detected electrons image cross-sections. Images of thin HEA6 and HEN2 films cross-sections are displayed in Figure 5. Average measured thicknesses values are given when multi marked bars are displayed and presented in Table 3.

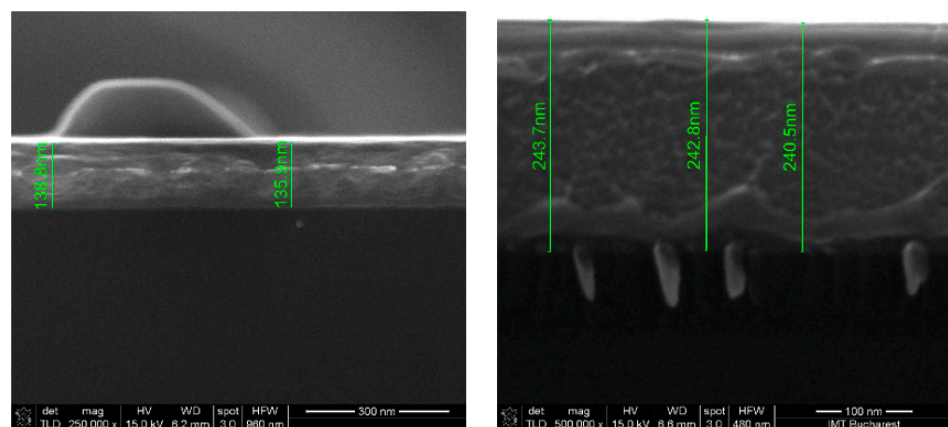


Figure 5. Cross-section obtained images of thin films and of their thicknesses which can be readable on marked bars of the HEA6 thickness $\sim 1.37 \times 10^{-7}$ m on the left side, and of the HEA2 thickness $\sim 2.32 \times 10^{-7}$ m on the right side.

The deposited films' elemental composition, estimated by means of EDS on one hand and XPS on the other, are displayed in Figures 6–8, as indicated.

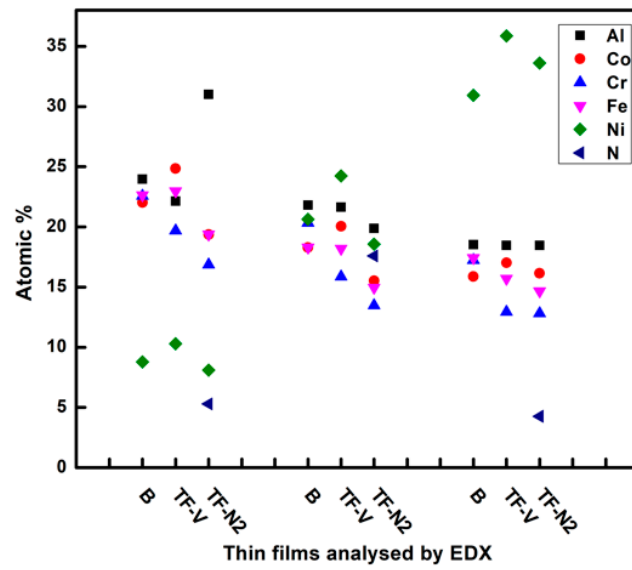


Figure 6. Plotted data on chemical elemental composition measurements by EDX of all HEAs bulk SS, and corresponding thin HEAs as well as HENs films of nickel concentration 0.4, 1.2, and 2.0. B stands for bulk, TF-V for thin HEA films, and TF-N2 for thin HEN films.

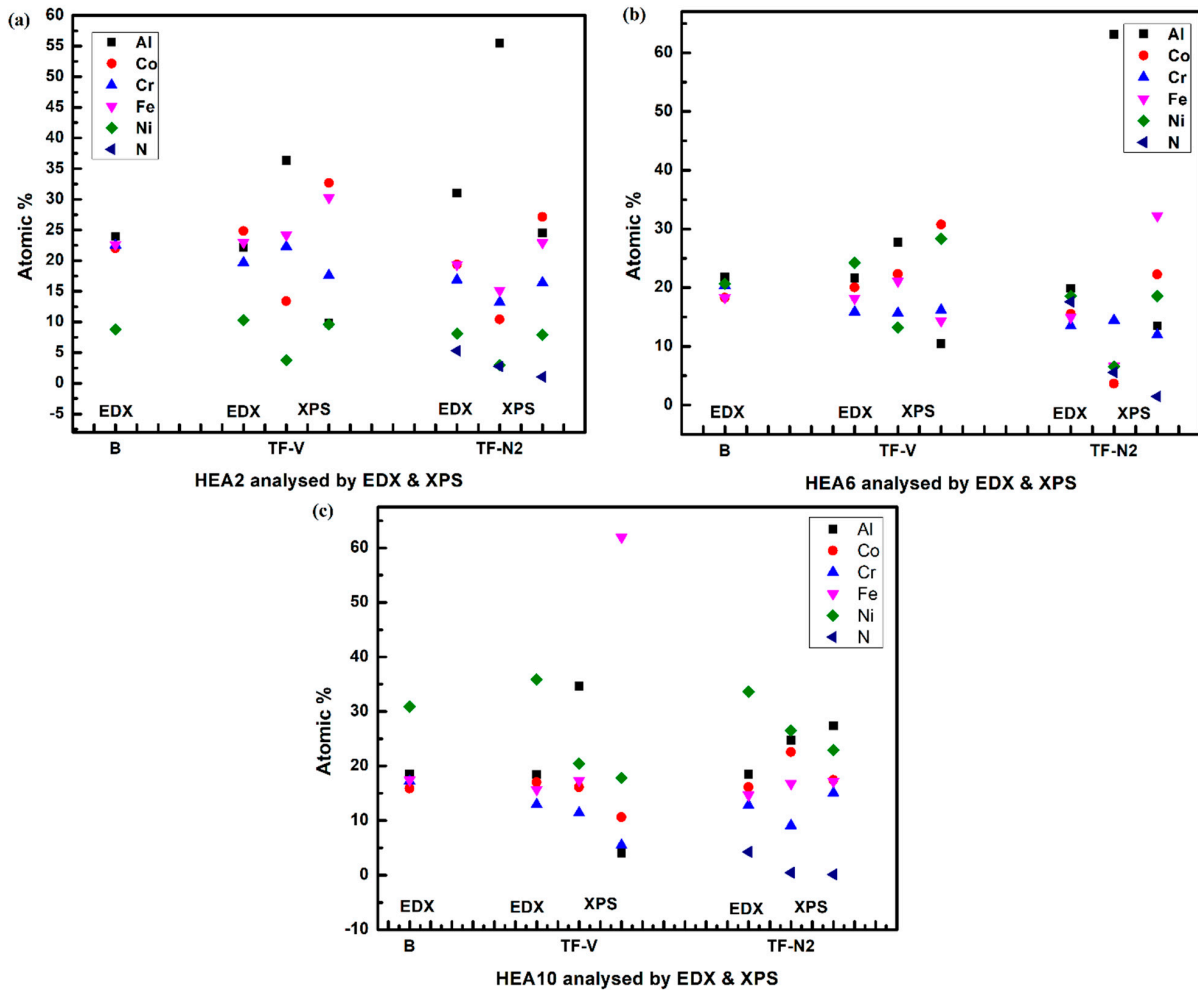


Figure 7. Plotted data on chemical elemental composition measurements by EDX and XPS of HEAs bulk SS, and corresponding thin HEAs as well as HENs films of nickel concentration of (a) 0.4, (b) 1.2, and (c) 2.0.

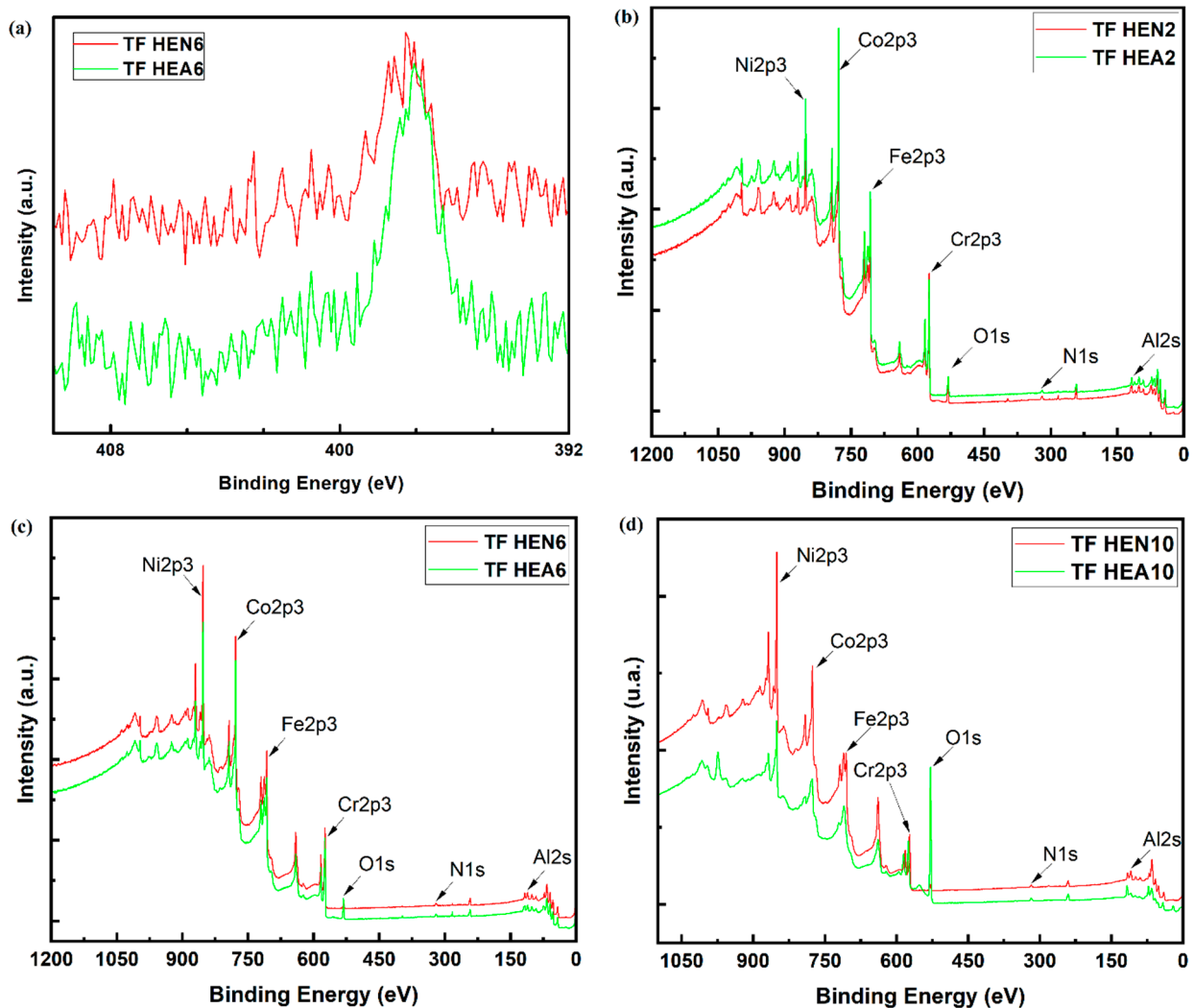


Figure 8. Plotted data on chemical elemental composition measurements by XPS of (a) N_2 content of the thin HEA and HEN films with nickel concentration 1.2, (b) overall analysis of the thin HEA and HEN films with nickel concentration 0.4, (c) overall analysis of the thin HEA and HEN films with nickel concentration 1.2, and (d) overall analysis of the thin HEA and HEN films with nickel concentration 1.8.

As a general trend, all mechanical parameters seem to decrease as the nickel content in the targets was increased. As far as the influence of the deposition atmosphere is concerned, except for the thin HEA and HEN films with a nickel molar ratio of 1.2 where the trend seems to be reversed, using an N_2 rich atmosphere leads to poorer mechanical characteristics, as shown in Figure 9. The resistance to elastic deformation, represented by the H/E ratio also displayed in Figure 9, has been used to predict the wear resistance of a material [16], a high H/E ratio often being a reliable indicator of good wear resistance of coatings. Consequently, the set of HEA2 samples should behave better during wear tests, followed by the set of HEA10. Furthermore, the H^3/E^2 ratio gives a relatively accurate description related to the capacity of a coating to dissipate energy when the film suffers plastic deformation [17].

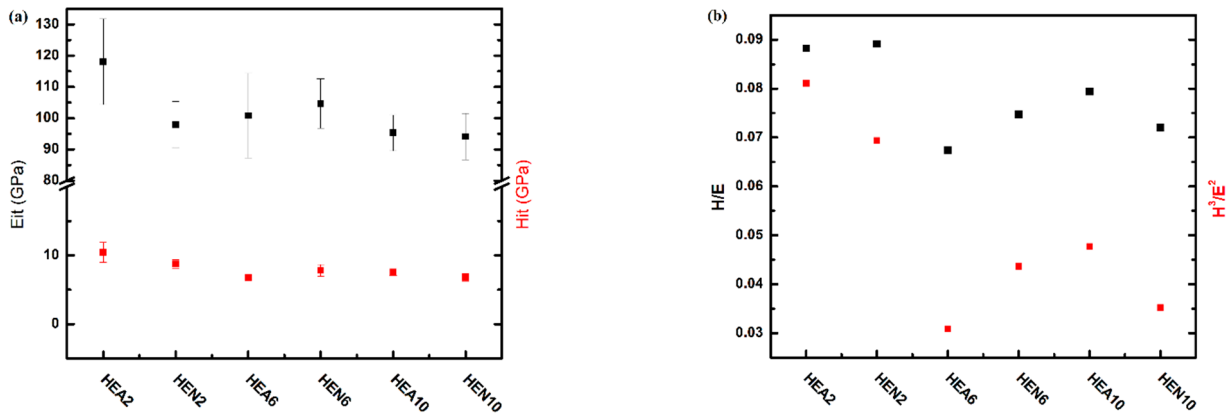


Figure 9. Plotted data on the variation of some measured mechanical characteristics: (a) hardness and elastic modulus, and (b) H/E ratio and H^3/E^2 ratio, both as function of HEA and HEN thin films, as obtained by instrumented indentation.

The adhesion of thin films to the substrate was assessed by micro-scratch testing. Figure 10 shows the variation of critical loads responsible for the first delamination on the scratch track (LC2), and the load responsible for total film removal (LC3). One can observe that these two critical loads were not present on all samples. The better behaviour was noticed for samples from the set of HEA10, at least in terms of total film removal. The thin film prepared in a vacuum atmosphere was not delaminated up to a 15 N maximum applied load. Increasing the applied load would lead to cohesive failure, the glass substrate fracturing under the applied load, which would not signify a loss of the thin film’s adhesion. Observing the optical micrographs from Figure 11, thin films seem to have a ductile nature, detaching from the substrate surface without exposing the substrate. This observation is in agreement with the relatively low hardness values. Considering the deposition atmosphere, it seems that for lower nickel content, samples deposited in nitrogen behave slightly better, exhibiting higher values for the LC3 critical load, compared to samples deposited in a vacuum. However, once the nickel content is increased (the set of HEA10), the trend is reversed.

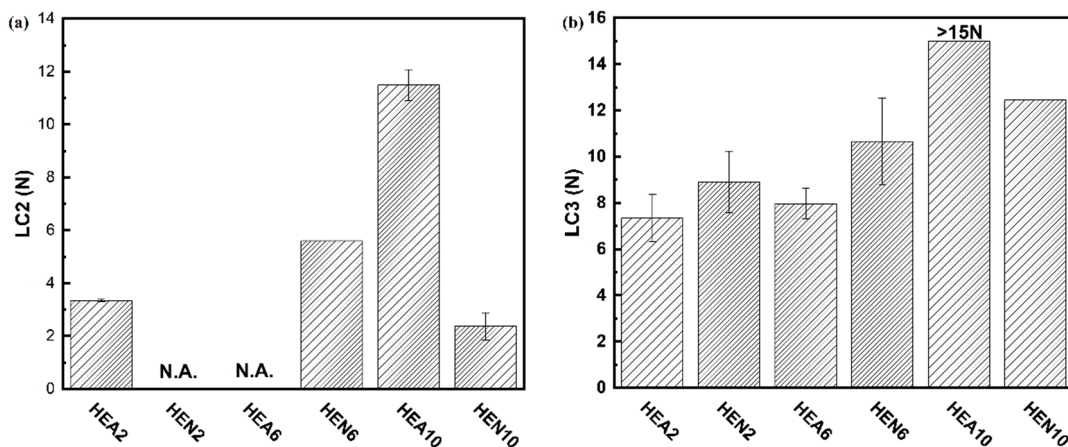


Figure 10. Plotted data on critical loads variation as function of sample characteristics: (a) LC2—the load necessary for the first delamination, and (b) LC3—the load responsible for total film removal.

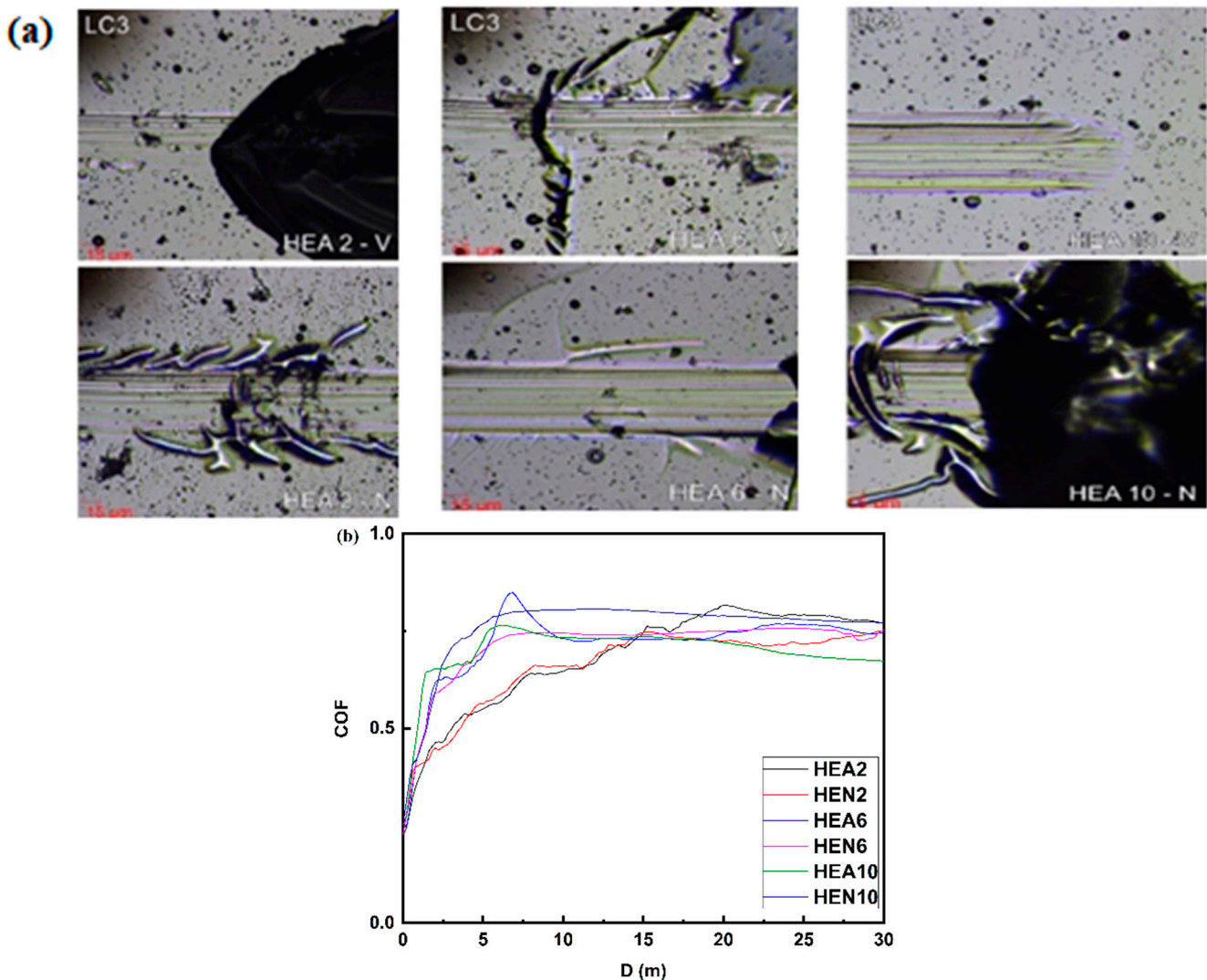


Figure 11. Obtained optical micrographs from scratch tests by critical load LC3 performed on (a) the thin HEA and HEN films with nickel concentration 0.4, 1.2, and 2.0 respectively, displayed on vertical from left to right, and (b) plotted data on the variation of the dynamic friction coefficient, as function of distance, obtained in dry conditions against Al_2O_3 balls.

4. Conclusions

This paper is an attempt to supplement the existing knowledge [18–21] regarding the effects of nickel addition on the obtainment of HEAs SS that were afterwards utilized to grow thin HEA and HEN films, as well as regarding their characteristics. Therefore, different batches were performed from the AlCrFeCoNi_x system with a nickel molar ratio x from 0.2 to 2.0 using the VAR technique. The mass of the ingots was 99.25%–99.77% of the initial total weight of the employed chemical materials. These values indicate that, during the elaboration process, elemental losses are minimal, caused by small splashes or vaporization, without significantly altering the chemical composition of experimental batches. The microstructure of as-cast alloy is dendritic. By increasing the nickel content, grain refinement can be observed, as well as a progressive decrease of the microhardness.

XRD analyses showed a target structural transition from a BCC (HEA2) to an FCC (HEA10) type lattice with the increase in nickel content. Films were deposited with a KrF laser under vacuum and N_2 atmospheres. Their structure was a mixture of FCC and BCC lattices for all targets used here. EDS analyses showed a good stoichiometric transfer from targets to thin films using the PLD technique. XPS analyses showed a

small difference in the elemental composition of each thin film set; it also showed the incorporation of nitrogen atoms into metallic nitride compounds. Measurements with a 4PP system found that a higher resistivity was measured for films deposited under an N₂ atmosphere. Nanoindentation measurements found that thin HEA2 and HEA10 films have the highest hardness and lowest elastic modulus values over their pairs of HEN thin films. However, this trend was reversed for thin HEA6 and HEN6 films, which showed higher values. A similar tendency was observed for the wear resistance of thin HEN over HEA films of pairs with a nickel molar ratio of 0.4 and 1.2 over those with a nickel molar ratio of 2.0. The trend in the capacity to dissipate energy when plastic deformation happens, of the HEAs over the HENs pairs of the pairs with nickel molar ratios of 0.4 and 2.0 over those with a nickel molar ratio of 1.2, which have the opposite values, was also observed. All samples reached the stable plateau (COF = 0.7–0.8) up to the 30 m mark, without any changes in the wear behaviour after this point. One can observe that the best behaving samples are the ones from set HEA2, which reached the stable plateau after approximately 15 m, while the remaining samples exhibited a stable friction coefficient much sooner. This phenomenon is in agreement with both the higher hardness of these samples, as well as with the higher H/E ratio values. There is no discernible influence of the deposition atmosphere on the wear behaviour, samples deposited in vacuum or those deposited in N₂ behaving similarly.

Author Contributions: Conceptualization, V.C. and E.A.L.; methodology, E.A.L.; software, E.A.L.; validation, E.A.L. and V.C.; investigation, D.C. (Doina Crăciun), G.D., V.G., I.V., D.C. (Daniel Cristea), G.C., E.A.L.; resources, V.C.; data curation, E.A.L.; writing—original draft preparation, E.A.L., V.C., D.C. (Doina Crăciun); writing—review and editing, E.A.L., V.G., I.V., D.C. (Doina Crăciun), V.C.; visualization, E.A.L., V.C.; supervision, V.C.; project administration, D.C. (Doina Crăciun); funding acquisition, V.C. All authors have read and agreed to the published version of the manuscript.

Funding: This work was supported by grants of the Ministry of Research, Innovation and Digitization, CCCDI—UEFISCDI, project number PN-III-P4-PCE-2021-1158 and PN-III-P2-2.1-PED-2021-0957, within PNCDI III.

Institutional Review Board Statement: Not applicable.

Informed Consent Statement: Not applicable.

Data Availability Statement: Not applicable.

Acknowledgments: Moreover, D.C. acknowledges the structural funds project PRO-DD (POS-CCE, O.2.2.1., ID 123, SMIS 2637, ctr. no 11/2009) for providing the CSM Instruments infrastructure used in this work, V.C. acknowledges the IFA-ELI grant ELI-RO-04/16.10.2020 and Nucleu programme LAPLAS VI, no. 16N/2019, and V.G. acknowledges the Romanian National Authority for Scientific Research, CNDI—UEFISCDI, through the project number PN-III-P2-2.1-PED-2019-3953, contract 514PED2020 “New ceramic layer composite material processed by laser techniques for corrosion and high temperature applications—LASCERHEA”, within PNCDI III.

Conflicts of Interest: The authors declare no conflict of interest.

References

1. Zhang, J.; Cai, C.; Kim, G.; Wang, Y.; Chen, W. Composition design of high-entropy alloys with deep sets learning. *NPJ Comput. Mater.* **2022**, *8*, 89. [[CrossRef](#)]
2. Nadzri, N.I.M.; Khemar, A.; Wahab, J.A.; Mahat, M.M. High Entropy Alloy Towards Functional Materials Application: A Review. *J. Phys. Conf. Ser.* **2022**, *2169*, 012007. [[CrossRef](#)]
3. Satyanarayana, M.B.; Yeh, J.-W.; Ranganathan, S.; Bhattacharjee, P.P. *High-Entropy Alloys*; Elsevier: Amsterdam, The Netherlands, 2019.
4. Fourth, E.; Ashby, M.F. *Material Selection in Mechanical Design*, 4th ed.; Butterworth-Heinemann Elsevier: Oxford, UK, 2011; ISBN 9780080952239.
5. Sheikh, S. Alloy Design and Optimization of Mechanical Properties of High-Entropy Alloys. Ph.D. Thesis, Chalmers Tekniska Hogskola, Gothenburg, Sweden, 2016.
6. Zhang, W.; Liaw, P.K.; Zhang, Y. Science and technology in high-entropy alloys. *Sci. China Mater.* **2018**, *61*, 2–22. [[CrossRef](#)]

7. Peter, I.; Rosso, M. Light alloys from traditional to innovative technologies. New Trends in Alloy Development. *Charact. Appl.* **2015**, *3*, 37.
8. Cantor, B.; Chang, I.T.H.; Knight, P.; Vincent, A.J.B. Microstructural development in equiatomic multi-component alloys. *Mater. Sci. Eng. A* **2004**, *375*, 213–218. [[CrossRef](#)]
9. Zhang, Y.; Zuo, T.T.; Tang, Z.; Gao, M.C.; Dahmen, K.A.; Liaw, P.K.; Lu, Z.P. Micro-structures and properties of high-entropy alloys. *Prog. Mater. Sci.* **2014**, *61*, 1–93. [[CrossRef](#)]
10. Chapelle, P.; Bellot, J.P.; Duval, H.; Jardy, A.; Ablitzer, D. Modelling of plasma generation and expansion in a vacuum arc: Application to the vacuum arc remelting process. *J. Phys. D Appl. Phys.* **2001**, *35*, 137–150. [[CrossRef](#)]
11. Tokarewicz, M.; Grządka-Dahlke, M. Review of Recent Research on AlCoCrFeNi High-Entropy Alloy. *Metals* **2021**, *11*, 1302. [[CrossRef](#)]
12. Zhang, Y.; Xing, Q. High Entropy Alloys: Manufacturing Routes. In *Reference Module in Materials Science and Materials Engineering*; Elsevier: Amsterdam, The Netherlands, 2020.
13. Agumba, O.J. Design and Fabrication of a Simple Four Point Probe System for Electrical Characterization of Thin Films. Ph.D. Thesis, Kenyatta University, Nairobi, Kenya, 2010.
14. Hertz, H. Ueber einen Einfluss des ultravioletten Lichtes auf die elektrische Entladung. *Ann. Phys.* **1887**, *267*, 983–1000. [[CrossRef](#)]
15. Einstein, A. On a heuristic point of view concerning the production and transformation of light. *Ann. Phys.* **1905**, 1–18. [[CrossRef](#)]
16. Leyland, A.; Matthews, A. On the significance of the H/E ratio in wear control: A nanocomposite coating approach to optimised tribological behaviour. *Wear* **2000**, *246*, 1–11. [[CrossRef](#)]
17. Tsui, T.Y.; Pharr, G.M.; Oliver, W.C.; Bhatia, C.S.; White, R.L.; Anders, S.; Anders, A.; Brown, I.G. Nanoindentation and Nanoscratching of Hard Carbon Coatings for Magnetic Disks. *MRS Proc.* **1995**, *383*, 447. [[CrossRef](#)]
18. López Ríos, M.; Perdomo, P.P.S.; Voiculescu, I.; Geanta, V.; Crăciun, V.; Boerasu, I.; Rosca, J.C.M. Effects of nickel content on the microstructure, microhardness and corrosion behavior of high-entropy Al-CoCrFeNi_x alloys. *Sci. Rep.* **2020**, *10*, 21119. [[CrossRef](#)]
19. Sim, R.K.; Xu, Z.; Wu, M.Y.; He, A.; Chen, D.L.; Li, D.Y. Microstructure, mechanical properties, corrosion and wear behavior of high-entropy alloy AlCoCrFeNi_x ($x > 0$) and medium-entropy alloy ($x = 0$). *J. Mater. Sci.* **2022**, *57*, 11949–11968. [[CrossRef](#)]
20. Tian, Q.W.; Zhang, G.J.; Yin, K.X.; Cheng, W.L.; Wang, Y.N.; Huang, J.C. Effect of Ni content on the phase formation, tensile properties and deformation mechanisms of the Ni-rich AlCoCrFeNi_x ($x = 2, 3, 4$) high entropy alloys. *Mater. Charact.* **2021**, *176*, 111148. [[CrossRef](#)]
21. Cao, L.; Wang, X.; Wang, Y.; Zhang, L.; Yang, Y.; Liu, F.; Cui, Y. Microstructural evolution, phase formation and mechanical properties of multi-component AlCoCrFeNi_x alloys. *Appl. Phys. A* **2019**, *125*, 699. [[CrossRef](#)]